CANCOM2024 – CANADIAN INTERNATIONAL CONFERENCE ON COMPOSITE MATERIALS

PREDICTIVE MODELING FOR DAMAGE AND RESIDUAL LOAD-BEARING CAPACITY OF NON-CRIMP FABRIC COMPOSITES

Kazemian, M.[1*] and Cherniaev, A.[1]
[1] Department of Mechanical, Automotive and Materials Engineering, University of Windsor, 401 Sunset Ave., Windsor, Ontario, Canada N9B 3P4
* Corresponding author (kazemiam@uwindsor.ca)
Keywords: *non-crimp carbon fabric; transverse crushing; damage modeling*

ABSTRACT

The study investigates the efficacy of two constitutive material models, LS-DYNA's MAT54 and MAT58, in predicting damage and residual load-bearing capacity of non-crimp fabric (NCF) components subjected to transverse crushing. These models, previously used for unidirectional and woven composites, are assessed through experimental and numerical analyses, including various material characterization tests and a two-phase testing procedure on NCF components. Despite formulation differences, both models can predict damage induced by transverse crushing in NCF parts, satisfactory replicating interlaminar damage patterns and force-displacement responses.

1 INTRODUCTION

Unidirectional non-crimp fabrics (NCFs) gained attention owing to their excellent mechanical properties and ease of production. These fabrics, comprising multiple straight and parallel yarn bands joined by polyester stitching, offer advantages over conventional UD tape composites. However, concerns persist regarding in-service damage, which can compromise structural integrity. [1-9]

Evaluating damage and residual load-bearing capacity in composite parts, regardless of reinforcement type, usually requires costly and time-consuming integration of experimental methods. A simulation approach suitable for this purpose would offer significant cost savings. [10-16]

This study assesses the effectiveness of commonly used material models, MAT54 and MAT58, available in commercial software, in simulating damage initiation and predicting load-bearing capacity in non-crimp fabric (NCF) elements. In this study, mechanical testing was conducted to characterize NCF material and measure residual load bearing capacity of pre-damaged representative structural components. Conducted LS-DYNA simulations replicated these experiments using MAT54 and MAT58 representations. By comparing results from the physical experiments and numerical simulations, the study aims to provide insights into the suitability and optimal utilization of these constitutive models for simulating NCF behavior.

2 EXPERIMENTAL TESTS

2.1 Material and Characterization

In this study, an intermediate modulus (IM) unidirectional non-crimp carbon fabric was employed, which had been pre-impregnated with epoxy resin. The fabric has an areal density of 140 g/m², with a resin content of 38±3%. Comprising 12K carbon fiber tows stitched together with a polyester binder, the fabric underwent a curing cycle as per the manufacturer's instructions. Subsequently, the flat specimens were subjected to electron microscopy analysis to explore their key features, such as fiber distribution, the cohesive zone between composite layers, polyester stitching, and the presence of resin-rich areas, which is depicted in Figure 1.

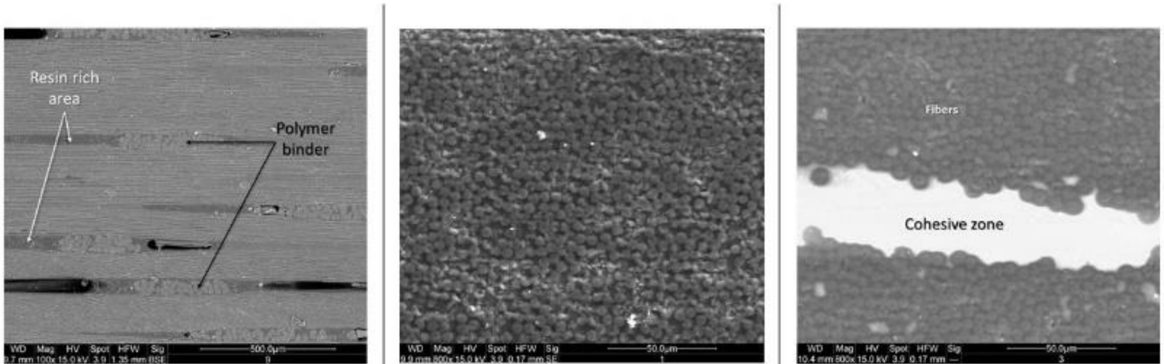

Figure 1- SEM for the NCF material a) stiches between the layers b) Fibers in bundle c) Cohesive zone between the layers.

The processed flat composite panels had in-plane dimensions of 100 x 300 mm, while the tubular specimens measured 200 mm in length, with internal cross-section dimensions of 25.4 mm x 25.4 mm. post-curing, the thickness of a single ply in the laminates was measured to be 0.15 mm. The flat panels of varying thickness were subsequently utilized for cutting test specimens, the parameters of which are detailed in Table 1. Digital image correlation (DIC) speckling was applied to all tensile test specimens (groups #1 – 3 in Table 1). The mechanical properties of the composite were obtained through post-processing of the test results, and these findings are shown in Table 2.

Table 1- Tests specimens for NCF mechanical characterization.

#	Test type	In-plane dimensions, mm x mm	Number of NCF layers	Test procedure
1	Longitudinal tensile test	250 x 15	8	ASTM D3039 [17]
2	Transverse tensile test	175 x 25	14	ASTM D3039 [17]
3	10°off-axis tensile test	250 x 15	8	Ref [18]
4	Double-cantilever beam (DCB) test (specimen with Teflon insert)	125 x 25	32	ASTM 5528b [19]
5	End-notched flexure (ENF) test (specimen with Teflon insert)	120 x 25	32	Ref [20]

Table 2- Mechanical properties of the unidirectional NCF material.

Property	**Units**	**Mean value**	**Property**	**Units**	**Mean value**
Longitudinal Young's modulus, $\mathbf{E_1}$	MPa	149018	In-plane shear strength, $\mathbf{S_L}$	MPa	44.5
Transverse Young's modulus, $\mathbf{E_2}$	MPa	6071	Longitudinal tensile strain-at-failure, $\boldsymbol{\varepsilon_{1f}}$	%	1.37
Major in-plane Poisson's ratio, $\boldsymbol{\nu_{12}}$	-	0.32	Transverse tensile strain-at-failure, $\boldsymbol{\varepsilon_{2f}}$	%	0.40
In-plane shear modulus, $\mathbf{G_{12}}$	MPa	4217	In-plane shear strain-at-failure, $\boldsymbol{\gamma_{12f}}$	%	1.71
Longitudinal tensile strength, $\mathbf{X_t}$	MPa	2060	Mode I strain energy release rate, G_{Ic}	$\mathrm{kJ/m^2}$	0.66
Longitudinal compressive strength*, $\mathbf{X_c}$	MPa	830	Mode II strain energy release rate, G_{IIc}	$\mathrm{kJ/m^2}$	2.77
Transverse tensile strength, $\mathbf{Y_t}$	MPa	29.1	Shear stress at onset of non-linearity	MPa	30
Transverse compressive strength*, $\mathbf{Y_c}$	MPa	126.6	Shear strain at onset of non-linearity	%	0.711

2.2 Component tests

In this study, a two-phase physical experiment was conducted. Initially, controlled indentation by a metallic cylinder was employed to induce damage in the structural components (phase I), followed by an assessment of the residual load-bearing capacity of the NCF tubes with the inflicted damage through four-point bending tests (phase II, Figure 2). The central loading of the tube by a cylindrical indenter led to localized deformation and damage in the NCF material, including fiber breakage, matrix cracking, delamination, and a reduction in cross-section in the middle of the tube (Figure 3). Detailed recordings of crosshead displacements and forces were made to facilitate comparison between these experimental findings and numerical simulation predictions for both phases. Additionally, X-ray computed tomography analysis of the layup was conducted to quantify the extent of induced damage and assist in the validation of numerical models. Selected outputs from the CT scans are depicted in Figure 4, illustrating the diverse failure modes experienced by the specimen.

Figure 2- The experimental setup.

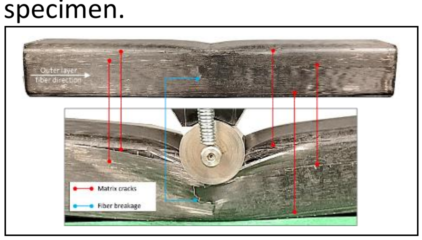

Figure 3- Visual damage – experiment

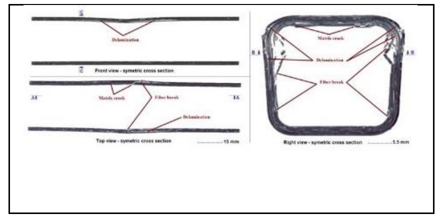

Figure 4- crushed specimen obtained using X-ray computed tomography.

3 NUMERICAL SIMULATIONS

3.1 Overall structure

In this study, an LS-DYNA numerical model was crafted to replicate the tubular component crushing test. Key features of the model are outlined in Figure 5, where the composite layup was represented using stacked TSHELL elements. Rigid body modeling was employed for both the support structure and the loading cylinders. Utilizing the MAT54 and MAT58 material models, the LS-DYNA explicit solver was utilized [21]. To enhance computational efficiency for quasi-static processes, the loading rate was increased from 0.5 mm/min to 2 m/s (the material models used were strain rate-independent). Additionally, only a half-section of the NCF tube was modeled to exploit geometric and loading symmetry, reducing simulation time. The developed numerical model incorporated the layup used in the physical experiments: $[0_4, 90_3]_S$

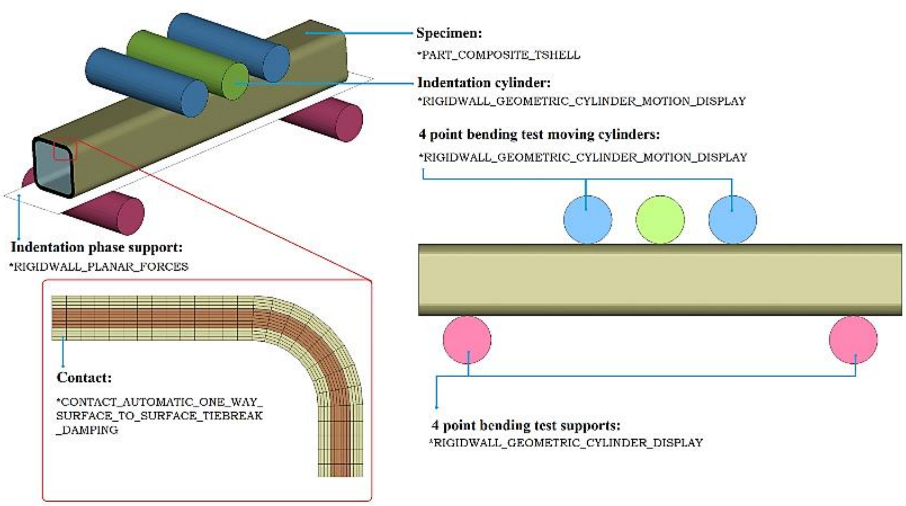

Figure 5- LS-DYNA numerical model.

3.2 Intera-Laminar damage simulation

MAT 54 and MAT 58 were utilized to characterize interlaminar behavior within the composite structure. MAT54 employs a strength criterion-based model, namely the Chang–Chang model, while MAT58 adopts a damage mechanics-based approach. Notably, MAT58 accounts for both pre- and post-peak softening of composite plies and provides formulations suitable for both UD tape and woven fabric. Both models share common features, including the incorporation of multiple non-physical parameters governing post-failure material behavior. The specific values assigned to these non-physical parameters are documented in Tables 3 for reference and reproducibility.

Table 3- The non-physical parameters for MAT 54 and MAT 58.

MAT54 – *MAT_ENHANCED_COMPOSITE_DAMAGE		
Parameter	**Units**	**Value**
TFAIL	s	1E-07
EPS	mm/mm	0.55
SOFT	–	0.90
SLIMT1	–	0.010
SLIMC1	–	0.375
SLIMT2	–	0.010
SLIMC2	–	0.375
SLIMS	–	1.000
FBRT	–	0
YCFAC	–	2.48

MAT58 – *MAT_LAMINATED_COMPOSITE_FABRIC		
Parameter	**Units**	**Value**
TFAIL	s	1E-07
ERODS	mm/mm	-0.55
SOFT	–	0.90
SLIMT1	–	0.010
SLIMC1	–	0.375
SLIMT2	–	0.010
SLIMC2	–	0.375
SLIMS	–	1.000

3.3 Delamination Simulation

The tube walls were modeled utilizing 14 layers of stacked TSHELL elements (TSHELL ELFORM 1 in LS-DYNA), with each layer representing a physical ply of the UD NCF material. To simulate delamination effects, contact interfaces were introduced between the 14 TSHELL layers using *CONTACT_AUTOMATIC_ONE_WAY_SURFACE_TO_SURFACE_TIEBREAK with OPTION 9. This contact algorithm effectively emulates zero-thickness cohesive zone elements and is grounded on a fracture model incorporating a bilinear traction-separation law, mixed mode delamination criterion, and damage formulation [22]. Key parameters of this delamination model are included in table 4.

Table 4- Input data for *CONTACT_AUTOMATIC_ONE_WAY_SURFACE_TO_SURFACE_TIEBREAK.

Property	NFLS	SFLS	G_Ic	G_IIc	CN	CT2CN
Unit	MPa	MPa	kJ/m^2	kJ/m^2	MPa/mm	-
Value	75.00	43.30	0.66	2.77	200,000	0.37

4 RESULT AND DISCUSSION

Criteria used for evaluating numerical predictions specific to the crushing phase included assessing the damage in the outer layer of the specimen (visual versus predicted), quantifying delamination extent (CT-scan versus models) and comparing force-displacement diagrams (experimental recordings versus those generated by LS-DYNA). The latter incorporates preliminary data from the second phase of testing, though this component is currently under investigation and may undergo subsequent adjustments.

The study utilized X-ray computed tomography to analyze a crushed tube model with a specific layup. The Porosity Analysis module of myVGL software was employed to visualize delamination areas within the tube, using the "Equivalent diameter" feature to represent defect size. Delamination in the model was depicted as contact gaps between TSHELL elements, with 13 ply interfaces considered for delamination display (Figure 5). Modeling results were adjusted for comparison with X-ray output. Comparison between experimental and predicted delamination regions showed similar extents, with around 26-27% of the specimen affected by delamination according to measurements.

Figure 3 illustrates the visual damage induced by crushing on the outer layer of the specimen, alongside predictions obtained using MAT54 (Figure 6) and MAT58 (Figure 7). Figure 3 reveals fiber breakage and multiple matrix cracks, particularly near the top and bottom surfaces in the central region and along the sides. MAT54 predicts longitudinal and transverse tensile and compressive failures but lacks a separate history variable for in-plane shear.

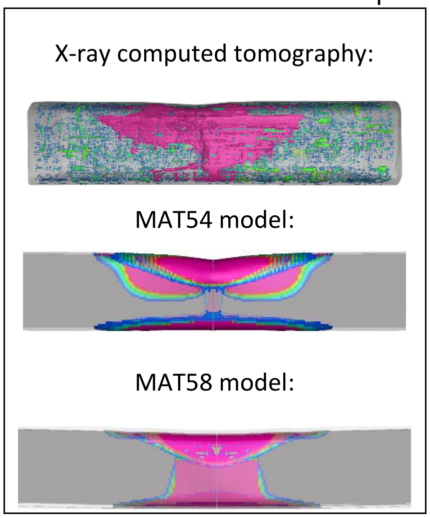

Figure 4- Delamination in the central 100 mm-long segment of the crushed specimen: CT-scan vs. numerical modeling.

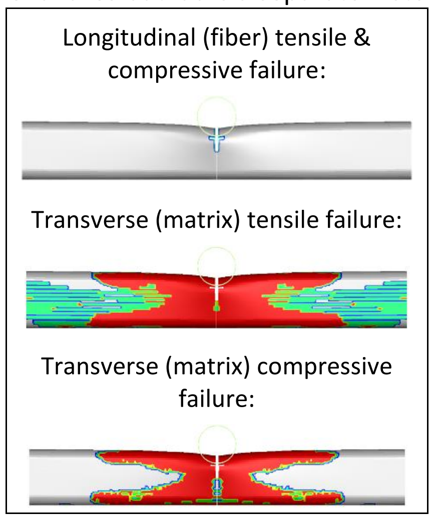

Figure 6- predicted (MAT54) damage in the outer layer of the specimen (color scheme: gray – not damaged, red – fully damaged; indenter shown for scale representation only).

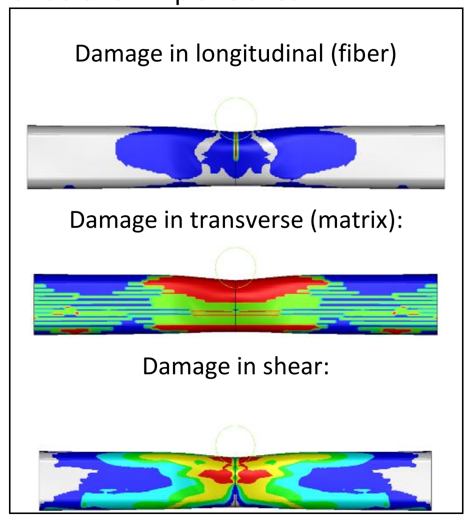

Figure 7- MAT58 predicted damage in the outer layer of the specimen (color scheme: gray – not damaged, red – fully damaged; indenter shown for scale representation only).

MAT58 predicts longitudinal, transverse, and shear damage without differentiating between tensile and compressive modes, showing gradual damage with fully damaged elements in the fiber direction and no erosion by the end of crushing. Both models qualitatively replicate the experimentally observed matrix cracking patterns.

The force-displacement diagrams for the crushing phase of the specimen, as depicted in Figure 8-a, compare the experimental results with the predictions from the constitutive models. Both MAT54 and MAT58 models adequately predict the force-displacement response during this phase.

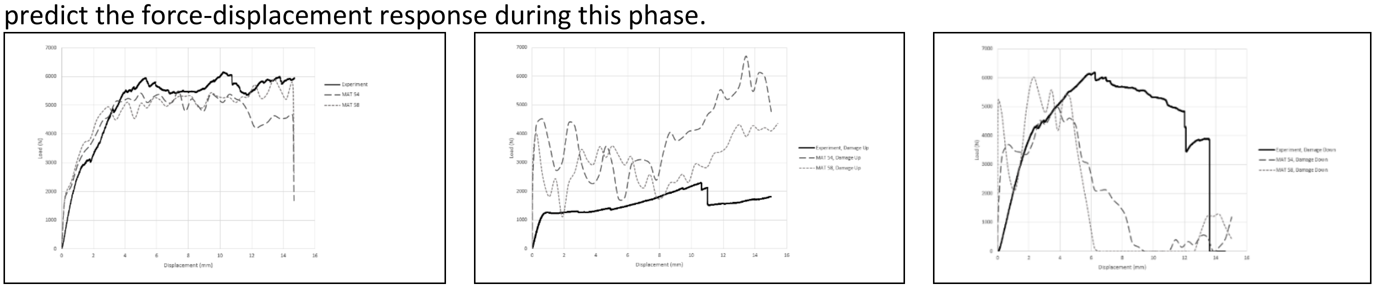

a) Indentation b) Damage Up c) Damage Down

Figure 8- Force-displacement diagrams: experiment vs. numerical modeling

For the subsequent phase, two sets of experiments were conducted: one with damaged area under compression and the other under tension. Although this part of the study is ongoing, preliminary results indicate that both models yield similar predictions, with MAT58 demonstrating slightly closer alignment with experimental data. Future research will further elucidate the accuracy of this assessment.

5 REFERENCES

[1] P. Middendorf and C. Metzner, "Aerospace application of non-crimp fabric composites," in Non-Crimp Fabric Composites, Philadelphia, Woodhead Publishing, 2011, pp. 441-449.
[2] B. Sköck-Hartmann and T. Gries, "Automotive applications of non-crimp fabric composites," in Non-Crimp Fabric composites, Philadelphia, Woodhead Publishing, 2011, pp. 461-480.
[3] G. Adolphs and C. Skinner, "Non-crimp fabric composites in wind turbines," in non-crimp fabric composites, Philadelphia, Woodhead publishing, 2011, pp. 481-493.
[4] T.-W. Shyr and Y.-H. Pan, "Impact resistance and damage characteristics of composite laminates," Composite structures, pp. 193-203, 2003.
[5] L. Greve and A. K. Pickett, "Modelling damage and failure in carbon/epoxy non-crimp fabric composites including effects of fabric pre-shear," Composites Part A: Applied Science and Manufacturing, pp. 1983-2001, 2006.
[6] S. V. Lomov, A. E. Bogdanovich, D. S. Ivanov, D. Mungalov, M. Karahan and I. Verpoest, "A comparative study of tensile properties of non-crimp 3D orthogonal weave and multi-layer plain weave E-glass composites. Part 1: Materials, methods and principal results," Composites Part A: Applied science and manufacturing, pp. 1134-1143, 2009.
[7] T. Segreto, A. Bottillo and R. Teti, "Advanced ultrasonic non-destructive evaluation for metrological analysis and quality assessment of impact damaged non-crimp fabric composites," Procedia CIRP, pp. 1055-1060, 2016.
[8] G. A. Bibo, P. J. Hogg, R. Backhouse and A. Mills, "Carbon-fibre non-crimp fabric laminates for cost-effective damage-tolerant structures," Composites Science and Technology, pp. 129-143, 1998.
[9] K. Berketis and D. Tzetzis, "The compression-after-impact strength of woven and non-crimp fabric reinforced composites subjected to long-term water immersion ageing," Journal of materials science, pp. 5611-5623, 2010.
[10] L. G. Zhao, N. A. Warrior and A. C. Long., "Finite element modelling of damage progression in non-crimp fabric reinforced composites," Composites Science and Technology, vol. 66.1, pp. 36-50, 2006.
[11] H. Yin, Q. Li and L. Iannucci, "Meso-scale Finite Element (FE) modelling of biaxial carbon fibre non-crimp-fabric (NCF) based composites under uniaxial tension and in-plane shear.," Composite Structures, vol. 290, p. 115538, 2022.
[12] K. Rouf, M. J. Worswick and J. Montesano., "A multiscale framework for predicting the mechanical properties of unidirectional non-crimp fabric composites with manufacturing induced defects," Journal of Composite Materials, vol. 55, no. 6, pp. 741-757, 2021.
[13] S. Costa, T. Bru, R. Olsson and A. Portugal., "Improvement and validation of a physically based model for the shear and transverse crushing of orthotropic composites," Journal of Composite Materials, vol. 53, no. 12, pp. 1681-1696, 2019.
[14] D. Gouskos and L. Iannucci., "A failure model for the analysis of cross-ply Non-Crimp Fabric (NCF) composites under in-plane loading: Experimental & numerical study," Engineering Fracture Mechanics, p. 108575, 2022.
[15] T. Senner, S. Kreissl, M. Merklein, M. Meinhardt and A. Lipp., "Bending of unidirectional non-crimp-fabrics: experimental characterization, constitutive modeling and application in finite element simulation.," Production Engineering, vol. 9, no. 1, pp. 1-10, 2015.
[16] A. Soto, E. V. González, P. Maimí, F. M. D. L. Escalera, J. S. D. Aja and E. Alvarez, "Low velocity impact and compression after impact simulation of thin ply laminates.," Composites Part A: Applied Science and Manufacturing, vol. 109, pp. 413-427, 2018.
[17] ASTM, "Standard Test Method for Tensile Properties of Polymer Matrix Composite Materials," Annual Book of ASTM standards, no. D3039/D3039M − 17, 2017.
[18] C.C. Chamis, and J. H. Sinclair, "10 Deg. off-axis Tensile Test for Intralaminar Shear," NASA TN D, p. 8215, 1976.
[19] ASTM, "Standard Test Method for Mode I Interlaminar Fracture Toughness of Unidirectional Fiber-Reinforced Polymer Matrix Composites1," Annual Book of ASTM, no. D 5528 – 01 (Reapproved 2007), 2007.
[20] L. A. Carlsson, D. F. Adams and R. B. Pipes, "Characterization of Delamination Failure," in Experimental characterization of advanced composite materials, Boca Raton, CRC Press;Taylor & Francis Group, 2014, pp. 250-262.
[21] Livermore Software Technology Corporation (LSTC), "LS-DYNA, ® Keyword user's manual volume II: material models," 2013.
[22] Livermore Software Technology Corporation (LSTC), "LS-DYNA, ® Keyword user's manual volume I," LSTC, Livermore, 2019